Smart Structures and Systems, *Vol. 35*, *No. 4* (*2025*) *177-194*
https://doi.org/10.12989/sss.2025.35.4.177

Compensatory evaluation of frequency evaluation metrics based on empirical mode decomposition

Weijie Xu [1a], Xiangjin Meng [1b], Tong Guo [1c], Changle Peng [1b] and Cheng Chen*[2]

[1] *Key Laboratory of Concrete and Prestressed Concrete Structures of the Ministry of Education*, *Southeast University*, *P.R. China*
[2] *School of Engineering*, *San Francisco State University*, *USA*

(*Received November 7*, *2024*, *Revised March 29*, *2025*, *Accepted April 16*, *2025*)

Abstract. Experimental evaluation is crucial for ensuring the accuracy of real-time hybrid simulation (RTHS) results. While existing methods can calculate time delay and amplitude error, time-varying delays can destabilize RTHS, requiring a method to account for them. This paper proposes using empirical mode decomposition (EMD) to calculate instantaneous control parameters, such as instantaneous amplitude and time delay. Intrinsic mode functions (IMF) from EMD capture the signal's local characteristics at different time scales, and the Hilbert transform is applied to compute these parameters. After EMD, a different number of IMFs may be obtained for calculated displacements than for measured displacements, and this paper gives advice on the IMFs needed to calculate instantaneous control parameters (ICP), and how they should be matched. The signals obtained from the numerical simulation of the benchmark model without and with compensation are firstly subjected to the calculation of ICP, and the results prove the effectiveness of ICP. Subsequently, the predefined displacement test with a multi-degree-of-freedom structure and the RTHS with a single-degree-of-freedom structure and self-centering viscous damper were subjected to the traditional ICP method and the EMD-based ICP calculation method for ICP calculation, respectively, and the comparative results show that the effectiveness of the EMD-based ICP calculation method is increased, and that EMD effectively solves the negative-frequency issue caused by signals with multiple poles between two crossed zeros. These calculations show great potential in improving experimental evaluations.

Keywords: empirical mode decomposition; instantaneous control parameters; instantaneous frequency; real-time hybrid simulation

1. Introduction

Real-time hybrid simulation (Nakashima *et al*. 1992) (RTHS) is an effective method for conducting large-scale dynamic tests within limited laboratory space, valuable for applications like structural seismic analysis (Stavridis and Shing 2010) and maglev train-guideway vibration studies (Wang *et al*. 2024). RTHS consists of two main components: the experimental substructure, used for physical testing of vulnerable or nonlinear components, and the numerical substructure, modeled via finite element analysis. These parts are synchronized through substructure interaction techniques. RTHS requires experiments to be conducted in real-time, necessitating efficient computational methods. Improving the integration algorithm can enhance computational efficiency and reduce computation time while maintaining stability and accuracy. The Chang algorithm (Chang 2002) builds on the Newmark algorithm by introducing two system parameters: displacement is handled explicitly, while velocity is managed using an implicit algorithm. Hayati and Song (2017) discussed the technical challenges of designing discrete-time compensators and proposed several optimal solutions to address these challenges. Phillips *et al*. (2014) proposed the backward difference method as an alternative to discretizing incorrect continuous time models for use as feedforward controllers in RTHS. Xu *et al*. (2023) proposed a model-based Kalman filter adaptive control strategy using a parameterized feedforward controller that is designed using a discrete inverse model of the control object and adjusted to displacement commands and measurements using Kalman filtering. Nakata and Stehman (2014) presents a set of techniques to enable reliable substructure shaker testing. These include compensation for errors caused by imperfect input accelerations to the shaker, model-based compensation of actuator delays using a state observer, and force correction for eliminating process and measurement noise.

The stability and accuracy assessment are important for RTHS for ensuring the credibility of the structure. However, time delays between commanded and measured displacements can disrupt this synchronization, compromising test accuracy and potentially destabilizing the experiment (Horiuchi *et al*. 1999). To prevent this, compensating for time delays is essential. Two common approaches to time delay compensation are direct

*Corresponding author, Ph.D., Professor,
E-mail: chcsfsu@sfsu.edu
[a] Senior Engineer
[b] Graduate Student
[c] Professor
[d] Graduate Student

ISSN: 1738-1584 (Print), 1738-1991 (Online)

displacement prediction and outer-loop actuator control theory-based methods. Recent advancements have introduced modern adaptive compensation methods. Despite these efforts, time delay cannot be fully eliminated, necessitating careful evaluation of experimental results. Various metrics, such as Maximum Tracking Error (MTE), Root Mean Square (RMS) error, Tracking Indicator (TI), and Energy Error (Mosqueda *et al*. 2007) (EE), are frequently employed, but they do not fully address the issue of time delay, making it difficult to assess the impact on RTHS outcomes.

Experimental evaluation is crucial when time delay cannot be fully compensated, Given the impact of time delay on these results, it is important to calculate the time delay during RTHS. Guo *et al*. (2014) proposed a frequency-domain evaluation indicators (FEI) to estimate the time delay and amplitude error. However, this metric only provides average values over the entire experiment. López and Moore (2024) proposed an enhanced adaptive linear transform to overcome the shortcomings when dealing with signal components with overlapping amplitudes. shortcomings when dealing with signal components with overlapping amplitudes, and well estimates the instantaneous amplitudes of different signals, especially those with intersecting frequencies. Huang *et al*. (2022) highlighted the instability caused by variable time delays, underscoring the need for moment-specific time delay measurements. Shirdade *et al*. (2024) also proposes a method of calculating instantaneous frequencies based on the fast Fourier transform and the wavelet transform, and demonstrates its accuracy. Li *et al*. (2024) developed a time-varying delay method for modulating and segmenting measured displacements. However, both methods have limitations, such as assumptions about delay ranges. Xu *et al*. (2024) later proposed a method to calculate instantaneous time delay and amplitude error using Hilbert transform (HT), but encountered issues with negative values in frequency calculation due to limitations of Bedrosian and Nuttall's theorem.

The concept of instantaneous frequency (IF) has undergone significant development since its inception. The first notable step was taken by Van der Pol (1946), a pioneer in the study of nonlinear systems, who thoroughly explored the idea of IF. Building on this, Gabor (1947) introduced the Hilbert transform to derive a unique analytic signal (AS) from real data, resolving the ambiguity of infinite possible combinations of amplitude and phase pairs used to represent a signal. For the AS method to yield physically meaningful Ifs, certain key conditions must be met: the function must be mono-component, locally zero-mean, and symmetric with respect to the zero mean (Huang *et al*. 2009). In recent years, there have been two major advancements in the computation of instantaneous frequencies. The first is the introduction of Intrinsic Mode Functions (IMFs), developed for analyzing nonlinear and non-smooth process data using the Empirical Mode Decomposition (EMD) method (Huang *et al*. 1998). The second involves wavelet decomposition, tailored for linear non-smooth process data (Olhede and Walden 2004). EMD is an adaptive method well-suited for processing non-linear, non-stationary time series, widely used in mechanical systems and signal processing (Gao *et al*. 2008, Guo *et al*. 2023). Maiti *et al*. (2024) used the IMF generated by Ensemble Empirical Mode Decomposition (EEMD) to create multiple datasets with multiple deep learning models and integrated predictions to forecast river flows. Van Jaarsveldt *et al*. (2023) demonstrated that the time-frequency resolution of EMD outperforms that of the fast Fourier and wavelet transforms, and clearly shows its value when dealing with the more challenging features present in time series. Park *et al*. (2022) combines EMD with empirical dynamic modeling (EDM) to improve prediction and discovery in the presence of noise or confusing observations. EMD decomposes a complex signal into a finite number of IMF, which ensure that there are no multi-polar points between the two zero crossing points in the data, addressing the problem of negative frequency calculation.

The structure of the paper is as follows: Section 2 details this new method for calculating instantaneous control parameters (ICP) based on EMD. Section 3 validates the method with numerically simulated signals from a benchmark model. Sections 4 and 5 present experimental results from predefined tests with multi-degree-of-freedom and single-degree-of-freedom structures, demonstrating that EMD effectively resolves the negative frequency issue. Finally, Section 6 summarizes the findings.

2. EMD based instantaneous control parameters

2.1 Empirical mode decomposition and intrinsic mode function

When processing signal using the Hilbert transform, negative frequencies may arise due to the presence of multiple poles between two over-zero points. Additionally, large amplitude fluctuations can contribute to these negative frequencies. To address this issue, Huang *et al*. (1998) introduced the concept of intrinsic mode functions (IMF), which must meet the following criteria: (1) , the number of extrema and zero-crossing points in the entire dataset must be equal or differ by at most one; (2) At any point, the average value between the envelope defined by local maxima and the envelope defined by local minima must be zero. The first condition help prevent negative frequencies caused by multiple poles, while the second condition reduces unnecessary fluctuations in instantaneous frequency caused from asymmetric waveforms. Therefore, using IMFs in Hilbert transforms can help mitigate negative frequencies to some extent. However, most data do not naturally meet the criteria for IMFs, making EMD necessary to decompose the signal and extract the IMFs. After EMD the input signal is decomposed into several eigenmode functions and a residual term. As follows

$$I(n) = \sum_{m=1}^{M} I\,MF_m(n) + Res_M(n) \tag{1}$$

where $I(n)$ denotes the input signal, $IMF_m(n)$ denotes the intrinsic mode function, and $Res_M(n)$ denotes the residual.

To obtain IMF through EMD, specific steps are

required. First, all local maxima and minima of the signal are identified. Then, cubic spline interpolation is employed to separately fit the upper and lower envelopes of the signal. Next, the mean curve of the upper and lower envelopes is calculated, and the remainder is addressed as a potential IMF. If the conditions for IMFs are met, the first IMF is obtained; otherwise, the procedure continues iteratively until the conditions are satisfied. This way, a regular signal can be decomposed into a series of IMFs, eliminating the negative frequencies when applying the Hilbert transform.

2.2 Instantaneous control parameters based on IMF in RTHS

Xu *et al*. (2024) proposed an Instantaneous Control Parameters (ICP) in real-time hybrid simulations which are defined as

$$IA_{xc}(t) = |z_{xc}(t)| = |s_{xc}(t) + jq_{xc}(t)| \quad (2a)$$

$$IA_{xm}(t) = |z_{xm}(t)| = |s_{xm}(t) + jq_{xm}(t)| \quad (2b)$$

$$IP_{xc}(t) = arg(z_{xm}(t)) = \arctan(q_{xc}(t)/s_{xc}(t)) \quad (2c)$$

$$IP_{xm}(t) = arg(z_{xm}(t)) = \arctan(q_{xm}(t)/s_{xm}(t)) \quad (2d)$$

$$IAD(t) = IA_{xm}(t)/IA_{xc}(t) \quad (2e)$$

$$IPD(t) = IP_{xm}(t) - IP_{xc}(t) \quad (2f)$$

$$IF(t) = \frac{1}{2\pi}\frac{dIP_{xc}(t)}{dt} \quad (2g)$$

$$ID(t) = -\frac{1}{2\pi}\frac{IPD(t)}{IF(t)} \quad (2h)$$

where *IA* and *IC* are the instantaneous amplitude and phase of the displacement, respectively; $z_{xc}(t)$ and $z_{xm}(t)$ are analytic signals of calculated displacement $xc(t)$ and measured displacements $xm(t)$ in RTHS after Hilbert transform, respectively; $s(t)$ and $q(t)$ represent the imaginary and real parts of the analytic signal, respectively; *IAD* and *IPD* are instantaneous amplitude difference and instantaneous phase difference, respectively; and *IF* and *ID* are instantaneous frequency and instantaneous delay, respectively.

In order to minimize the effect of high-frequency noise on the computation, zero-phase filtering is performed first before EMD.

$$Y(\omega) = X(\omega) \cdot H(\omega) \quad (3a)$$

$$H(\omega) = |H(\omega)| \cdot e^{j\phi(\omega)} \quad (3b)$$

where $X(\omega)$ is the original signal spectrum, $Y(\omega)$ is the output signal spectrum obtained after filtering, and $H(\omega)$ is the frequency response of the filter. The amplitude response and phase response are included, where the phase response of the filter is zero, i.e., $\phi(\omega)$ is zero, so that all frequency components of the signal do not have any phase shift after filtering.

Zero-phase filtering is performed as follows: first the signal is forward processed through a filter to obtain an intermediate result; the forward processed result is inverted and processed again through the same filter; and inverted again to obtain the final result.

$$y_f^R[n] = y_f[N - 1 - n] \quad (4a)$$

$$y_b^R[n] = H[n] \cdot y_f^R[n] \quad (4b)$$

where $y_f[n]$ is the result after forward filtering, $y_f^R[n]$ is the inverted signal, and N is the length of the signal. $y_b^R[n]$ is the result after forward filtering; this result is inverted to obtain $y_b[n]$, which is the zero-phase filtered output. Eq. (3a) represents the inversion signal process and Eq. (3b) represents the filtering process.

The proposed computational method involves two steps for optimization: phase unwrapping and asynchrony correction for the calculated and measured displacements. In addition, parameters for evaluating effective *IF* and *ID* are proposed

$$R^{IF} = \frac{n^{IF}}{n^{total}} \times 100\% \quad (5a)$$

$$R^{ID} = \frac{n^{ID}}{n^{total}} \times 100\% \quad (5b)$$

where n^{IF}, n^{ID}, n^{total} are the numbers of effective *IF*, effective *ID* and total data. In Eq. (5). Effective *IF* and *ID* are determined by pre-estimating their range. Values falling within this range are considered valid; otherwise, the value from the last instant is used.

In general, negative frequencies are considered invalid. Additionally, the time delay, defined as the ratio of phase difference to frequency, can become excessively large at very low frequencies. Therefore, in this paper, only frequencies greater than 0.1 Hz are deemed valid. Similarly, a large phase difference can lead to inaccurate time delay calculations, so a limit on the phase difference is applied to exclude such inaccuracies. For uncompensated cases, the *ID* typically does not exceed 50 msec. For a 5 Hz structure, the average time delay d is 0.05 s. The *IPD* is calculated as follows: $IPD = -2\pi \cdot f \cdot d = -2\pi \times 5 \times 0.05 = -\pi/2$. In this case, without compensation, the time delay is positive, but the IPD should be negative. Thus, if the *IPD* is not within the range $(-\pi/2,0)$ or if the *IF* is below 0.1, the *ID* is considered invalid, and the value from the previous time step is retained instead of recalculating. For the compensated case, the *ID* is based on a delay of 10 ms. Using the same 5 Hz structure, the average time delay d is 0.01 s. The IPD is computed as: $IPD = -2\pi \cdot f \cdot d = -2\pi \times 5 \times 0.01 = -\pi/10$. Since compensation can be either positive or negative, if the *IPD* is not within the range $(-\pi/10, \pi/10)$ or if the IF falls below 0.1 Hz, the ID is again considered invalid and is not recalculated; the value from the previous moment is utilized instead.

However, this calculation method is still prone to negative frequencies. Therefore, it becomes necessary to

utilize IMFs to address the negative frequencies when calculating ICP. Before applying Eqs. (1a) to (1h), both the calculated and measured displacements must undergo EMD to extract their respective IMFs. If the calculated displacement is decomposed into n IMFs, they are denoted as x_{c1}, x_{c2}, x_{c3},…, x_{cn}. Similarly, if the measured displacement is decomposed into m IMFs, they are denoted as x_{m1}, x_{m2}, x_{m3},…, x_{mm}. Instead of analyzing the original displacements (x_c and x_m), the IMFs (x_{c1}, x_{c2}, x_{c3},…, x_{cn}, x_{m1}, x_{m2}, x_{m3},…, x_{mm}) are examined using their instantaneous control parameters. These parameters are weighted to derive the new ICP, which addresses any negative instantaneous frequencies. However, a challenge arises when the number of IMFs obtained from the calculated displacements differs from those of the measured displacements, even after filtering out high-frequency noise.

Traditionally, ICP is calculated by comparing one calculated displacement with one measured displacement. However, following EMD, multiple IMFs are produced for both calculated and measured displacements. Direct use of these IMFs for ICP calculation is not feasible, as a one-to-one correspondence between the IMFs is required. To achieve this, a correlation coefficient is introduced. This coefficient is calculated between each IMF of *xc* and *xm*, enabling the matching of IMFs for ICP calculation. The methodology for this computation is described in two scenarios. Additionally, when matching IMFs for computation, the correlation coefficient between the IMFs of the combined *xc* and *xm* is calculated to reflect the relationship between the decomposed IMFs and the original signals. If the difference between this correlation coefficient and that of the original signals *xc* and *xm* is less than 5%, the use of EMD is recommended. However, if the error exceeds 5%, the computed result may not accurately represent the relationship between the original signals.

2.2.1 xc and xm yield same numbers of IMFs

When *xc* and *xm* have the same number of IMFs, i.e., $n = m$, the IMFs with higher correlation coefficients between *xc* and *xm* are used to separately calculate their ICPs. These parameters are then weighted to meet the criteria for evaluating the performance of RTHS. In this case, the IMFs of *xc* and *xm* generally correspond, meaning the correlation coefficient is maximized for the same layer of *xc* and *xm*. As a result, the ICPs for each IMFS can be directly calculated by substituting xc_i and xm_i into Eq. (1a) for the ith IMF. However, when n or m becomes too large, the significance of the IMFs diminishes due to the endpoint effect. Consequently, the correlation coefficient no longer maintains a consistent maximum value, and often decreases significantly. Therefore, it is recommended to disregard ICP calculations when the absolute maximum correlation coefficient falls below 0.5.

2.2.2 xc and xm yield different numbers of IMFs

When *xc* and *xm* yield different numbers of IMFs after EMD, the correspondence between IMFs of *xc* and *xm* may not be evident. In this case, the displacement with fewer IMFs is taken as the reference. Subsequently, the correlation coefficients between the IMFs of the other displacement and the reference IMFs are computed. The IMFs are derived using the IMFs that show higher correlation coefficients, which are then substituted into *xc* and *xm* before applying Eq. (1a). The process involves calculating the correlation coefficients between each IMF of signal *xc* and all IMFs of signal *xm*, and then ranking them based on the strength of these coefficients. Assuming $n < m$, the IMFs of *xm* are matched to those of *xc*, e.g., when x_{ci}, $x_{mi} = x_{margmax\{cov(xci,xm(i=1:m))\}}$. This method helps filter out high-frequency noise and irrelevant IMF components caused by endpoint effects.

2.3 Weighting method for different IMF

To ensure accurate results, it is essential to appropriately weigh these different IDPs. In calculating the ICP from various IMFs, this study applies a weighting scheme that evaluates each IMF based on its coefficient correlation with the filtered signal. The correlation coefficient indicates the degree of correlation between the IMF component and the original data, and is calculated for xc using the following equation

$$\rho = \frac{\mathrm{cov}(\mathrm{xc}', \mathrm{xci})}{\sigma_{xc'}\sigma_{xci}} = \frac{E\left[\left(xc'\text{-}\mathrm{E}(\mathrm{xc}')\right)\left(xci\text{-}\mathrm{E}(\mathrm{xci})\right)\right]}{\sigma_{xc'}\sigma_{xci}} = \frac{E(xc'xci)\text{-}\mathrm{E}(xc')E(xci)}{\sqrt{E\left(xc'^2\right)\text{-}\mathrm{E}^2(xc')}\sqrt{E(xci^2)\text{-}\mathrm{E}^2(xci)}} \tag{6}$$

The close ρ to 1, the stronger the correlation between the component and the original data. A high ρ suggest that the IMF component captures a significant portion of the information in the original signal, making it a crucial component. Conversely, a low ρ implies that the IMF component explains less of the original signal, potentially signaling it as noise or less important component. The weighting formula is as follows

$$IF = \sum_{i=1}^{n} I\,F_i \times \rho_i \tag{7a}$$

$$ID = \sum_{i=1}^{n} I\,D_i \times \rho_i \tag{7b}$$

where IF_i is the IF calculated for each IMF, ID_i is the ID calculated for each IMF, and ρ_i is the correlation parameter between each IMF and the original signal.

2.4 Procedure of EMD based instantaneous control parameters

Fig. 1 shows the computation process of EMD-based IDPs, which involves the following steps:

- Step 1: Filter calculated and measured displacements. Apply zero-phase filtering to both the xc and xm signals. Zero-phase filtering is utilized to reduce noise in the signals while preserving their frequency characteristics without introducing phase delay.

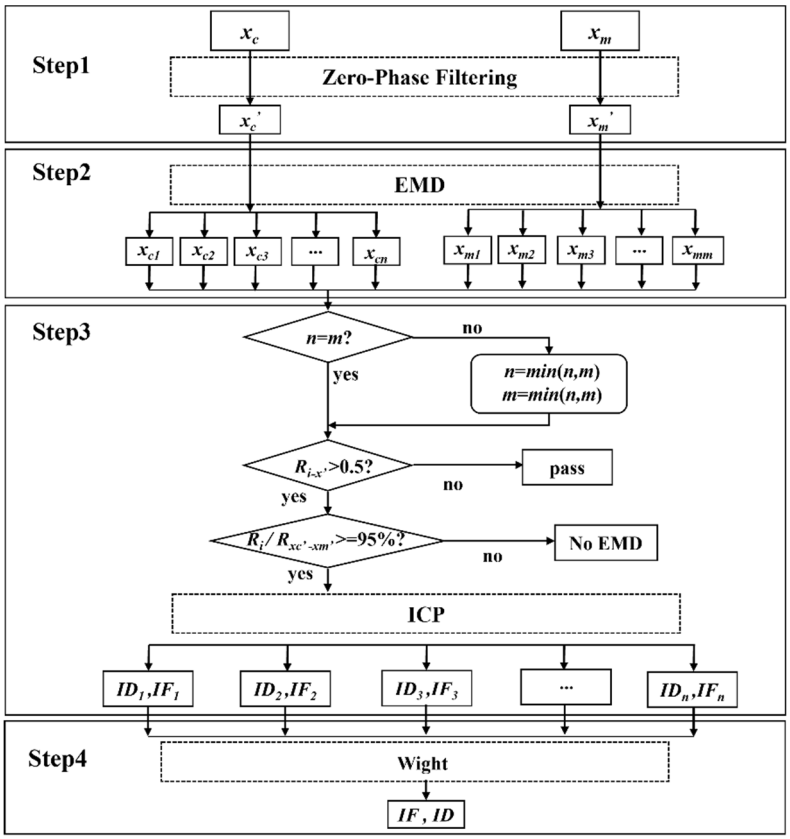

Fig. 1 Procedure of EMD based instantaneous control parameters calculation

- Step 2: Perform EMD to obtain IMF. Using the MATLAB's cubic Hermite interpolation method, EMD is applied to decompose the signals into sets of IMFs, denoted as xc1, xc2, xc3,…, xcn, xm1, xm2, xm3,…, xmm, instead of single xc and xm components. These IMFs are then used in subsequent calculations.
- Step 3: Calculate ICP under each IMF based on weights. The goal is to match the sets of xc1, xc2, xc3,…, xcn and xm1, xm2, xm3,…, xmm prior to computing the ICPs. This is achieved by computing the correlation coefficients between IMFs and selecting with higher correlations for the ICP calculation. Based on these selected combinations, multiple ICP values are computed. Additionally, it is recommended to omit correlation coefficients Ri-x' when they fall below 0.5; and the correlation coefficient Ri between matched IMFs or Rxc' -xm' between xc and xm that have an error greater than 5% should be excluded from the EMD process.
- Step 4: Calculate overall ICP based on weights. The correlation coefficients between the IMF and the filtered signals are used as weights. These weights are applied to the individual ICP calculations to derive the final ICP.

3. Application of traditional instantaneous control parameters in benchmark model

3.1 introduction of benchmark model

Condori Uribe *et al*. (2023) introduced a novel maRTHS benchmark model illustrated in Fig. 2(a), where the model comprises a steel moment-resisting frame featuring 3 bays and 3 stories. Notably, the bottom midspan serves as an experimental substructure, while the remainder is treated as a numerical substructure. Within the experimental substructure, two supplementary components are integrated to alter its dynamics. Couplers facilitate the synchronization of linear strokes from two actuators, ensuring equivalent translational and rotational motion. Fig. 2 (b) gives a visual representation of the primary components.

3.2 RTHS without compensation

The calculated and measured displacements obtained from the simulation using the uncompensated benchmark model were utilized to calculate the instantaneous time delay and validate the method's feasibility. The time delay curve is shown in Fig. 3(a), with a close-up view in Fig. 3(b) covering 7 to 7.3 seconds. As observed in Fig. 3(b), a distinct phase difference corresponding to the time delay is clearly observed. The overall picture of the phase difference can be seen in Fig. 3(c) for the *xc-xm* curve, which shows a curve dispersed around a 45-degree straight line, and it is clear that *xc* has a significant phase difference with *xm*. To

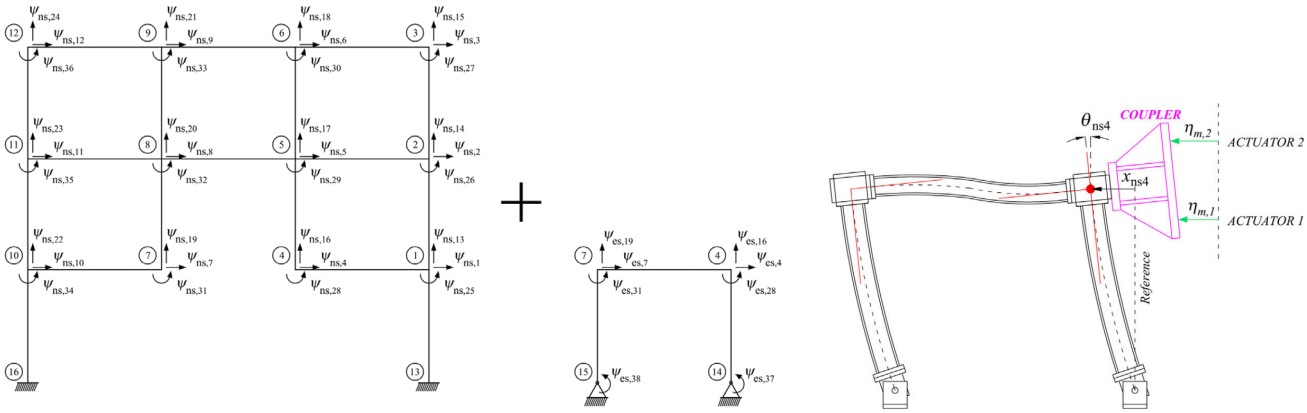

(a) Partitions of the benchmark model (b) Load pattern of the experimental substructure

Fig. 2 Composition of the benchmark model

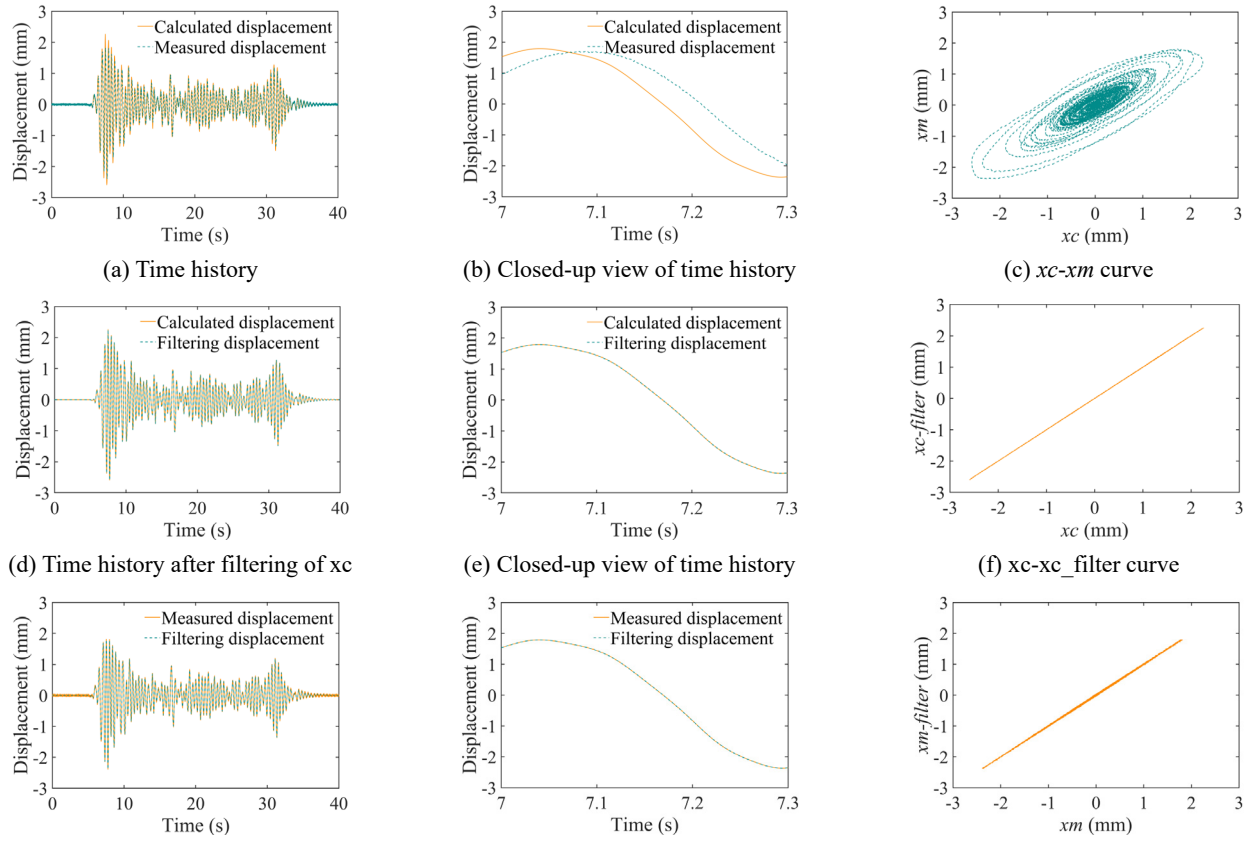

(a) Time history (b) Closed-up view of time history (c) *xc-xm* curve

(d) Time history after filtering of xc (e) Closed-up view of time history (f) xc-xc_filter curve

(g) Time history after filtering of xm (h) Closed-up view of time history (i) xm-xm_filter curve

Fig. 3 Time history of the original signal and the filtered post-signal

reduce the high-frequency noise present in the displacements calculated by the baseline model, zero-phase filtering was applied. This effectively minimized the noise's impact on subsequent calculations. Fig. 3(d) presents the time-history curves of the calculated and filtered displacements. Fig. 3(e) provides a close-up view from 7 to 7.3 seconds, showing the alignment between calculated and filtered displacements. Fig. 3(f) shows the *xc-xc_filter* curve, showing a 45-degree straight line, and it is clear that *xc* has no significant phase difference from *xc_filter*. Fig. 3(g) shows the time-history curves of the measured and filtered displacements, where the filtered displacements exhibit reduced high-frequency noise, particularly noticeable in the flattened segments during the initial 5 seconds and final 7 seconds. Fig. 3(h) offers a close-up view of the 7 to 7.3-second period, confirming that the filtering did not introduce any phase shift. Fig. 3(i) shows the *xm-xm_filter* curve, showing a 45-degree straight line, and it is clear that *xm* has no significant phase difference from *xm_filter*.

The analysis using the FEI yielded an average amplitude of 0.895 and a time delay of 40.26 ms over the entire test.

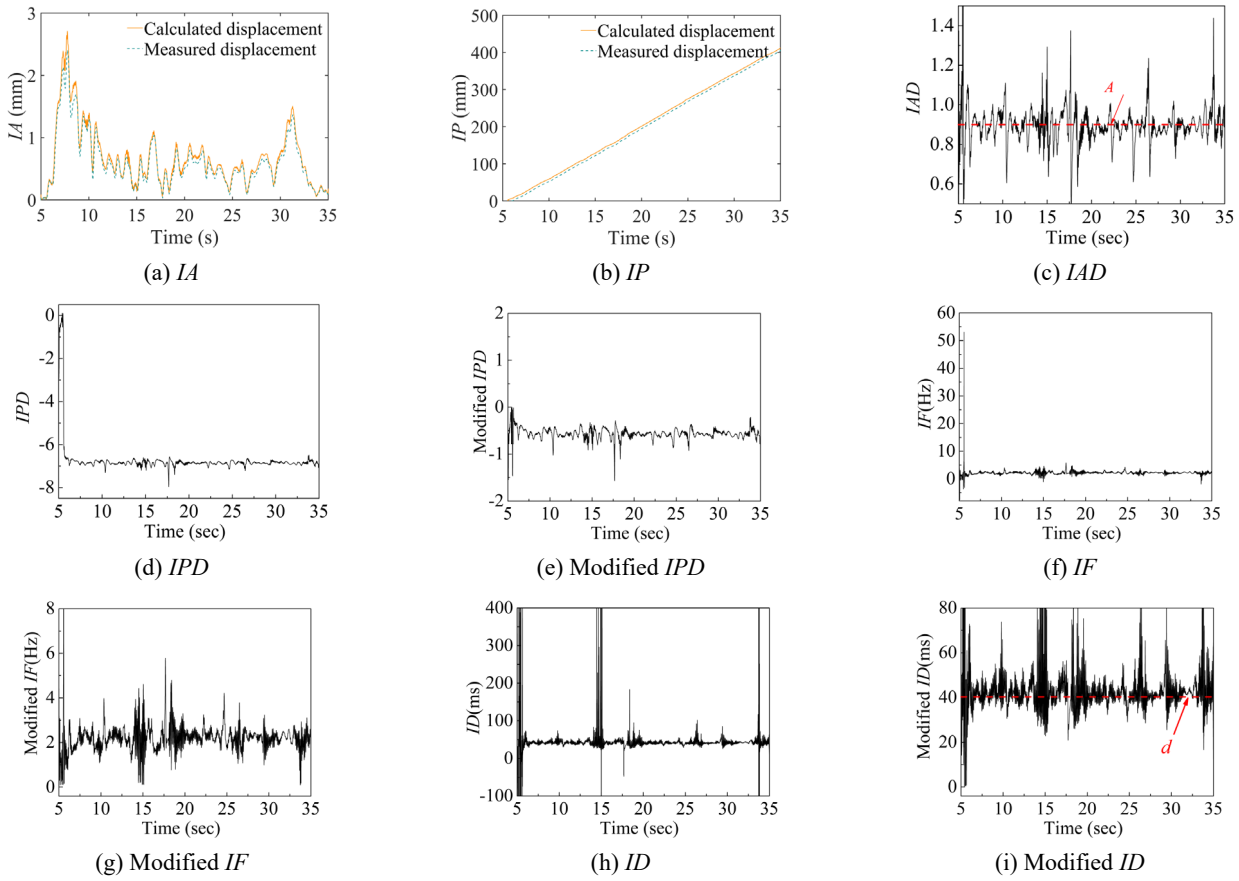

Fig. 4 ICPs for the RTHS without compensation

Since the displacement of the signal during the first 5 seconds and the last 7 seconds is minimal—resulting in lower potential damage and greater calculation error during these periods—only the time interval from 5 to 35 seconds was considered for the analysis. The *IA* and *IP* are shown in Figs. 4(a) and 4(b). The IA corresponds to the maximum displacement in the time course, while the *IP* shows a slight phase difference, due to asynchrony in phase unfolding, which must be corrected in subsequent calculations.

The *IAD* and *IPD* are illustrated in Figs. 4(c) and 4(d). The FEI analysis also yields an average amplitude of 0.895 for this simulation, as shown by the red line *A* in Fig. 4(c). The maximum and minimum *IAD* values, 5.6 and 0.3, occurring at 5.55 seconds and 5.58 seconds, respectively, both during moments of extremely small *IA*. Excluding the periods with very small *IA* at the beginning and end of the interval, most *IAD* values range between 0.8 and 1.0, fluctuating around the average amplitude difference calculated by FEI. The *IPD* stabilizes around -6.8, which should fall within the expected range of $(-\pi/2, 0)$. Adjustments were made, and the corrected *IPD* is shown in Fig. 4(e). Fig. 4(f) presents the calculated *IF* based on the *IP* of the calculated displacement, with values ranging from -7.5 Hz to 53 Hz, the maximum occurring at 5.55 seconds and the minimum at 5.05 seconds. Fig. 4(g) shows the corrected *IF*, with negative frequencies removed. The corrected IF (R^{IF}) is 99.25% of the computed IF values (30492 points) fall within the expected range. Fig. 4(h) shows the calculated *ID*, with values ranging from -2.86 seconds to 4 seconds. The maximum occurs at 5.04 seconds, and the minimum at 5.36 seconds, both corresponding to times when the *IF* is very small. Fig. 4(j) presents the corrected *ID*, which fluctuates between 30 ms and 50 ms. The average time delay *d* calculated by FEI is shown in Fig. 4(i), demonstrating that the instantaneous time delay fluctuates around this value. The corrected ID (R^{ID}) is 98.69% of the *ID* results (30317 points) fall within the expected range.

3.3 RTHS with the Nonlinear Autoregressive with External Input model (NARX) model-based compensation

Using the displacement data obtained from the NARX benchmark model simulation and the measured results, the instantaneous time delay was calculated to assess the method's feasibility of the method. The time-history curves are shown in Fig. 5(a), and the close-up views from 7 to 7.3 seconds in Fig. 5(b) span. To mitigate the high-frequency noise inherent in the displacements computed by the benchmark model, a zero-phase filter was applied to minimize the effect of this noise on subsequent computations. Fig. 5(c) shows the *xc-xm* curve, showing a 45-degree straight line, and it is clear that *xc* has no significant phase difference from *xm*. Fig. 5(d) compares the time histories of the computed and filtered displacements, while Fig. 5(e) zooms in on the 7 to 7.3 second range, highlighting the alignment between the two.

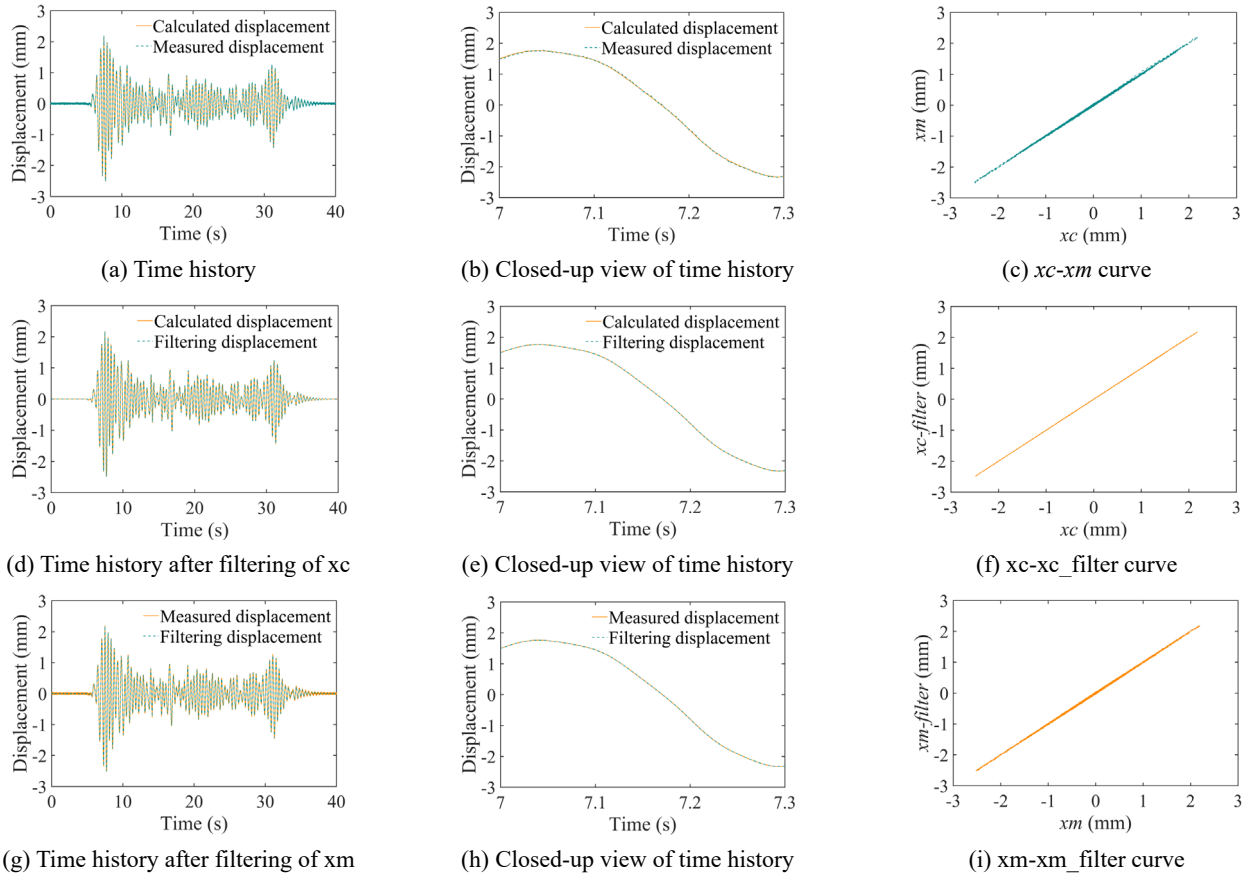

(a) Time history (b) Closed-up view of time history (c) *xc-xm* curve

(d) Time history after filtering of xc (e) Closed-up view of time history (f) xc-xc_filter curve

(g) Time history after filtering of xm (h) Closed-up view of time history (i) xm-xm_filter curve

Fig. 5 Time history of the original signal and the filtered post-signal

Fig. 5(f) shows the *xc-xc_filter* curve, showing a 45-degree straight line, and it is clear that *xc* has no significant phase difference from *xc_filter*. Fig. 5(g) presents the measured displacement against the filtered displacement, where the reduction in high-frequency noise is notable, especially in the flattened segments during the first 5 and last 7 seconds. Fig. 5(h) confirms that the filtering did not alter the phase. Fig. 5(i) shows the *xm-xm_filter* curve, showing a 45-degree straight line, and it is clear that *xm* has no significant phase difference from *xm_filter*.

Analysis using the FEI yielded an average amplitude difference and time delay of 0.999 and 0.07 ms, respectively, over the entire test, with a lower *IF* limit of 0.1 Hz. Figs. 6(a) and 6(b) present the *IA* and *IP*, respectively. The instantaneous amplitude reflects the maximum displacement over time, while the *IP* shows a slight phase difference due to asynchrony during phase unfolding, which requires subsequent adjustment. Figs. 6(c) and 6(d) present the *IAD* and *IPD*. The FEI analysis yields an average amplitude of 0.999 for this simulation, represented by the red line A in Fig. 6(c). The *IAD* reaches maximum and minimum values are 3.4 and 0.5 at 5.55 s and 5.56 s, respectively, both during periods of low *IA*. Most *IAD* values fall between 0.95 and 1.05, fluctuating around the FEI-calculated average amplitude. The *IPD* stabilizes near -6.3, correlating with the IP in Fig. 6(b). For numerical simulation of the compensation, the IPD is expected to fluctuate around zero, and in this case, it has been adjusted to fall within the range [-π/10, π/10], as shown in Fig. 6(e). Fig. 6(f) shows the computed *IF* based on the *IP* of the calculated displacement. The IF values range from -4 Hz to 57 Hz, with a maximum at 5.55 s and a minimum at 5.05 s. Fig. 6(g) shows the corrected IF, where negative frequencies have been eliminated. The R^{IF} is 98.73% (with 30,331 points within range), indicating that 98.73% of IF values fall within the acceptable range. In Fig. 6(h), the calculated ID values range from -34.7 s to 1.17 s, with a maximum at 5.46 s and a minimum at 5.17 s, both occurring at very low IF values. Fig. 6(i) shows the corrected ID, which primarily fluctuates between -2 ms and 2 ms. Additionally, Fig. 6(j) represents the average time delay, *d*, calculated by FEI, with the instantaneous time delay fluctuating around *d*. The R^{ID} is 98.40% (with 30,230 points within range).

The numerical simulation results using the benchmark model without compensation show that the R^{IF}, obtained without applying EMD, is 99.25%, while the R^{ID} is 98.69%. In comparison, the benchmark model with NARX compensation achieves an R^{IF} of 98.73% and an R^{ID} of 98.40%. These metrics suggest that *ICP* calculations hold considerable promise for experimental validation. Furthermore, since these metrics demonstrate sufficient robustness and the issue of negative frequencies is minimal, the application of EMD may not be necessary. The effectiveness of EMD will, however, be evaluated in future experiments.

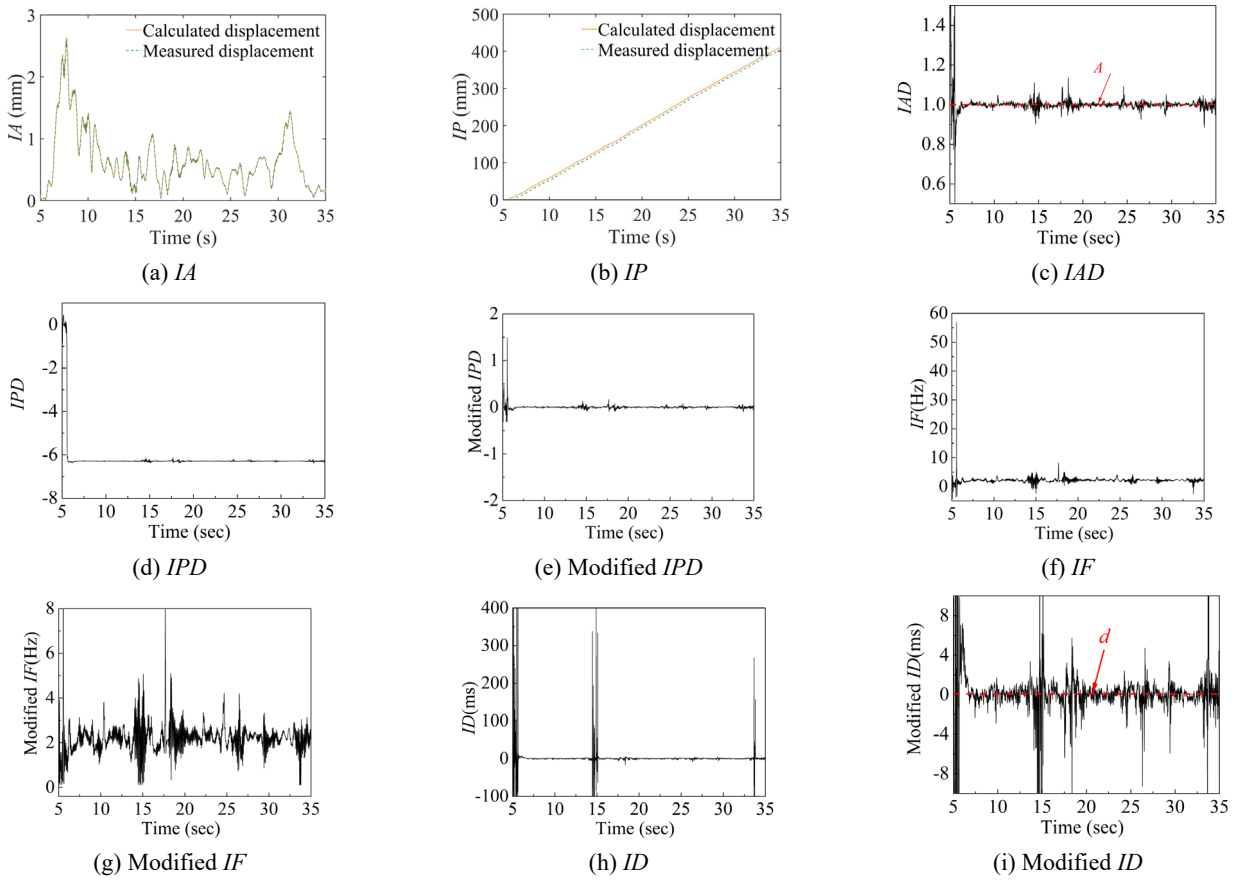

Fig. 6 ICPs for the RTHS with NARX model

4. Experimental Verification through real-time predefined test

4.1 Experimental setup and traditional ICP results for real-time predefined test

Laboratory tests were further conducted at the Key Laboratory for Concrete and Prestressed Concrete Structures, Ministry of Education, Southeast University, to experimentally evaluate the effectiveness of the program. As shown in Fig. 7, the test setup consisted of two steel reaction frames, an actuator, a spring for predefined displacement tests, and a damper for real-time hybrid simulation (RTHS). The MTS 244.21 servo-hydraulic actuator had a load capacity of 50 kN and a displacement stroke of ±75 mm. The spring had a stiffness of 40 kN/m. The actuator was controlled by an MTS FlexTest100 controller mounted on a host PC with a sampling rate of 1024 Hz.

The numerical substructure of a two-story, four-bay steel moment-resisting frame was modeled using the open-source software RT- Frame 2D (Castaneda *et al*. 2015), as shown in Fig. 8 with beam and column sections. Nonlinear beam-column elements were employed, with concentrated plastic hinges to capture the frame's nonlinear behavior.

The experimental substructure featured self-centering viscous dampers (SCVDs). To ensure a significant contribution to the restoring forces, each floor was equipped with 40 dampers. Assuming uniform displacement across each floor, the restoring force measured from the laboratory-tested dampers was multiplied by 40 to represent the total force generated by all dampers. To introduce

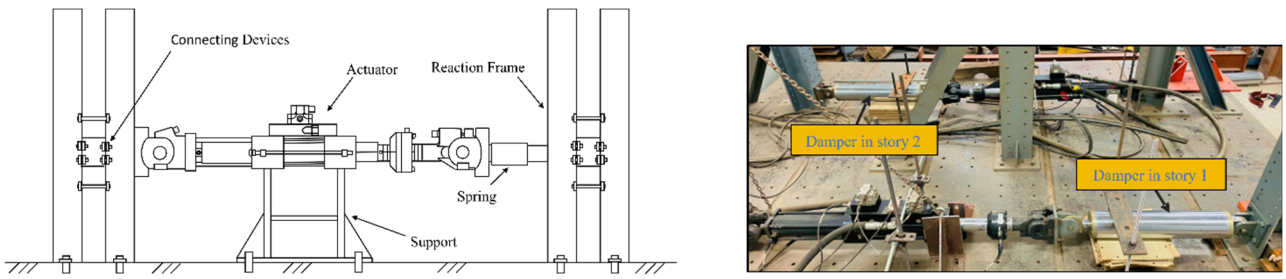

(a) Sketch of the experimental setup (b) Physical diagram of the experimental setup

Fig. 7 Experimental setup for tests

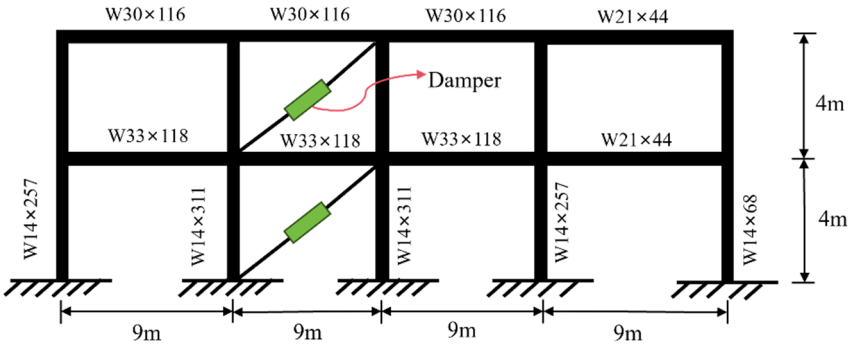

Fig. 8 Schematics of 2-story steel moment resisting frame with SC-VDs

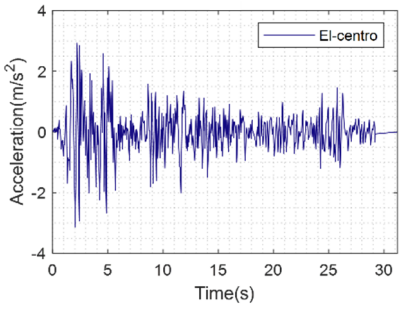

Fig. 9 Ground motion acceleration history

pronounced nonlinearity into the numerical substructure of the steel frame, ground motion was scaled to a peak ground acceleration (PGA) of 6 m/s², as illustrated in Fig. 9. At this level, the inter-story drift exceeds 1/200, warranting the consideration of frame nonlinearity effects. The structural dynamics were solved using the unconditionally stabilized explicit CR algorithm (Chen and Ricles 2008), and a recently developed NARX compensation technique was employed to mitigate the influence of servo-hydraulic dynamics. Additionally, the experiment utilized a neural network model, which applied predefined displacements derived from whole-structure simulation calculations.

4.2 Predefined displacements test

4.2.1 Predefined displacements test without EMD

Fig. 10(a) presents the predefined displacements test, with a close-up view from 9 to 9.5-second in Fig. 10(b). Zero-phase filtering was again applied to reduce the impact of high-frequency noise on subsequent calculations. Fig. 10(c) shows the *xc*-*xm* curve, showing a 45-degree straight line, and it is clear that *xc* has no significant phase difference from *xm*.

Figs. 11(a) and 11(b) display the IA and IP, respectively, where the clockwise amplitude corresponds to the maximum displacement in the time course. Figs. 11(c) and 11(d) show the IAD and IPD. The FEI analysis yields an average amplitude difference of 1.003 for this simulation, as indicated by the red line A in Fig. 11(c). The maximum and minimum IAD values, 2.88 and 0.32, occur at 22.59 s and 0.53 s, respectively, both coinciding with periods of extremely low IA. Excluding the initial moments of very low IA, the majority of IAD values are concentrated between 0.95 and 1.05, fluctuating around the FEI-calculated average amplitude difference, A. Fig. 11(e) presents the calculated IF based on the IP of the computed displacement, with values ranging from -5 Hz to 54 Hz. The maximum IF occurs at 19.6 s and the minimum at 22.6 s. Fig. 11(f) shows the corrected IF, where negative frequencies are removed, resulting in an R^{IF} of 92.95% (28,553 points within range), indicating that 92.95% of the IF values fall within the acceptable range. Fig. 11(g) illustrates the calculated ID, which ranges from -71.2 s to 3.7 s, with the maximum at 0.24 s and the minimum at 0.58 s, both occurring when the IF is very small. Fig. 11(h) displays the corrected ID, which predominantly fluctuates between -10 ms and 10 ms. Additionally, the average time delay, *d*, calculated by the FEI, is 0.336, as shown in Fig. 11(h), with the instantaneous time delay fluctuating around *d*. The R^{ID} is 92.90% (28,539 points within range).

4.2.2 Predefined displacements test with EMD

After EMD, *xc* produces 6 IMFs and *xm* produces 7 IMFs. Figs. 12(a) and 12(b) show the 3 IMFs of the displaced signals after EMD, and since the correlation

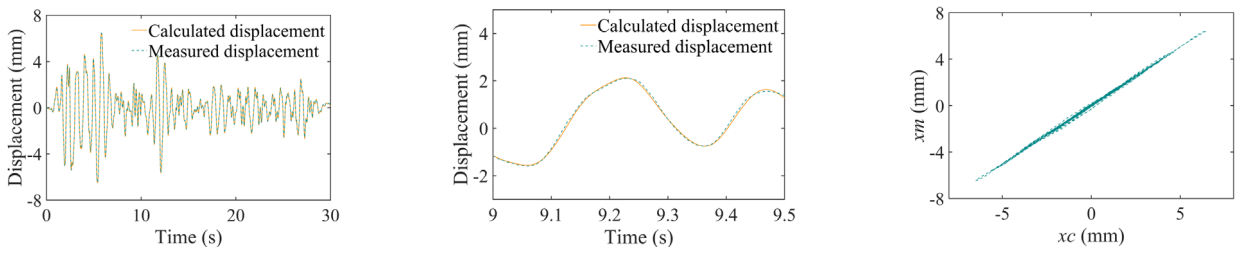

(a) Time history (b) Closed-up view of time history (c) *xc*-*xm* curve

Fig. 10 Time history of the signal

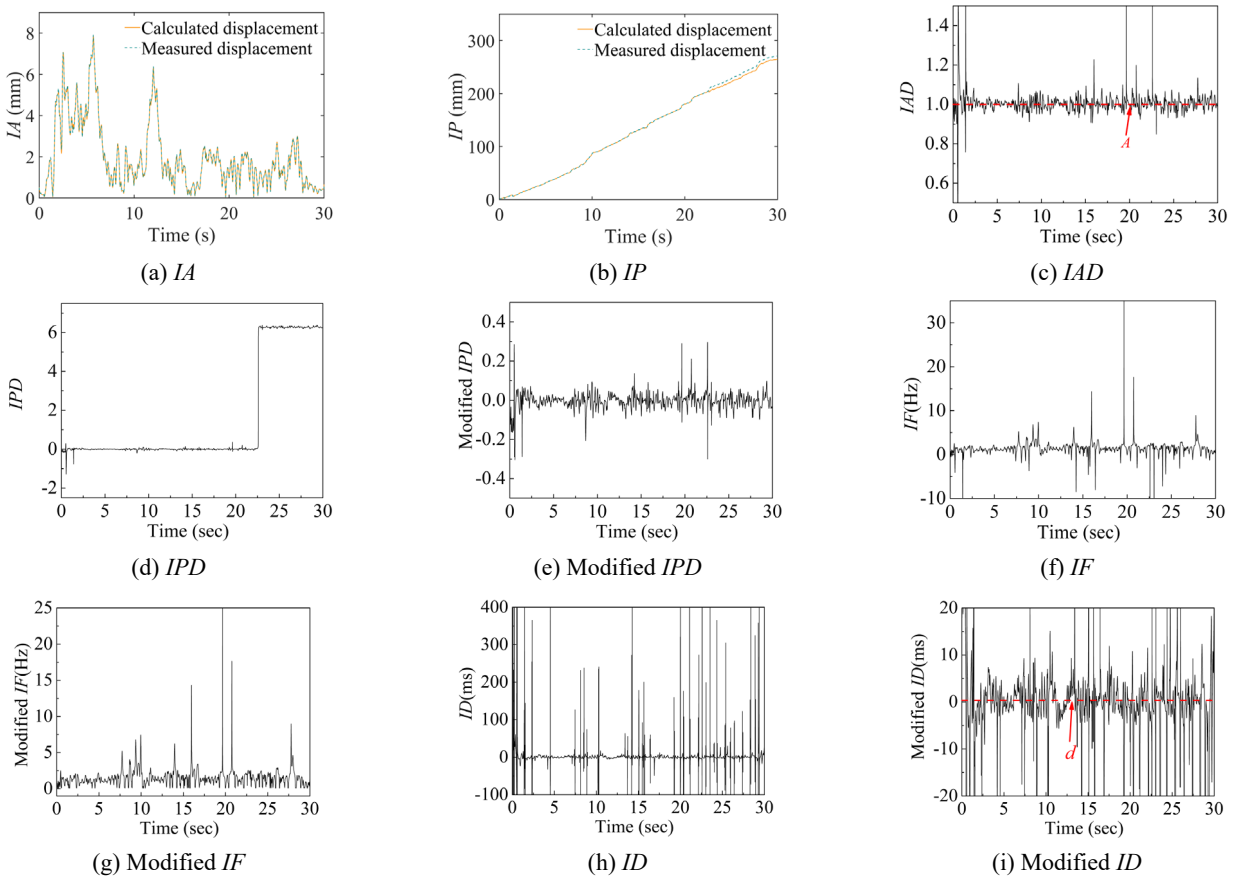

Fig. 11 ICPs for the predefined displacements test without EMD

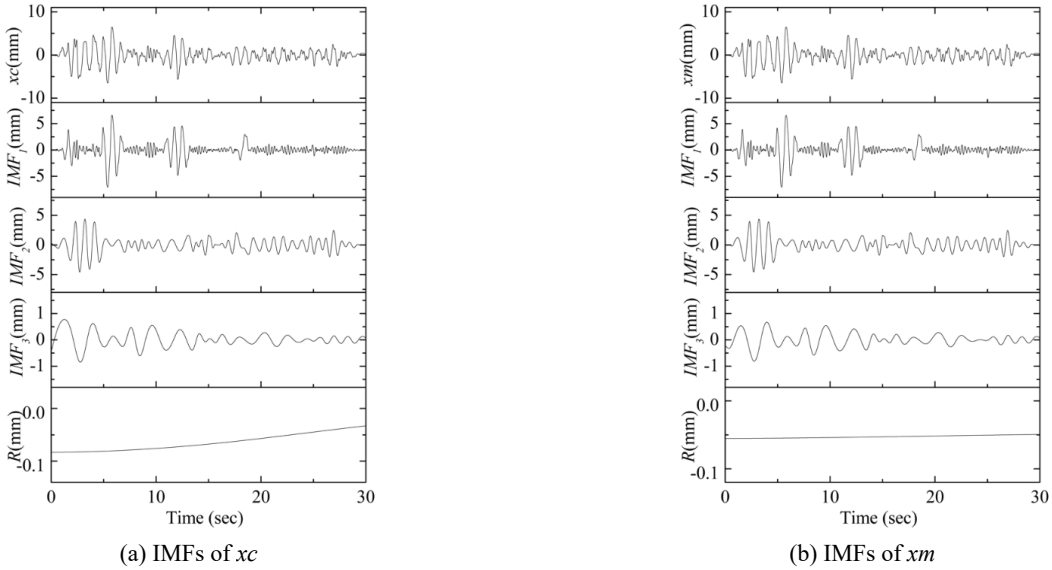

Fig. 12 IMFs obtained after EMD

coefficients of the subsequent IMFs are too small, only 3 IMFs are shown, and the correlation coefficients of the three of these IMFs with the original signals are 0.73, 0.60, and 0.19, respectively. Ultimately, only the top two IMF is chosen for the perform the ICP calculation. The correlation coefficient between *xc* and *xm* is 0.999, the correlation coefficient between IMF_1 is 0.998, the correlation coefficient between IMF_2 is 0.997, the inheritance is good enough to use EMD.

Figs. 13(a) and 13(b) present IA_1 and IP_1 where the clockwise amplitude corresponds to the maximum displacement over time. IAD_1 and IPD_1 are shown in Figs. 13(c) and 13(d). The FEI analysis yields an average amplitude of 1.003 in this simulation, as indicated by the

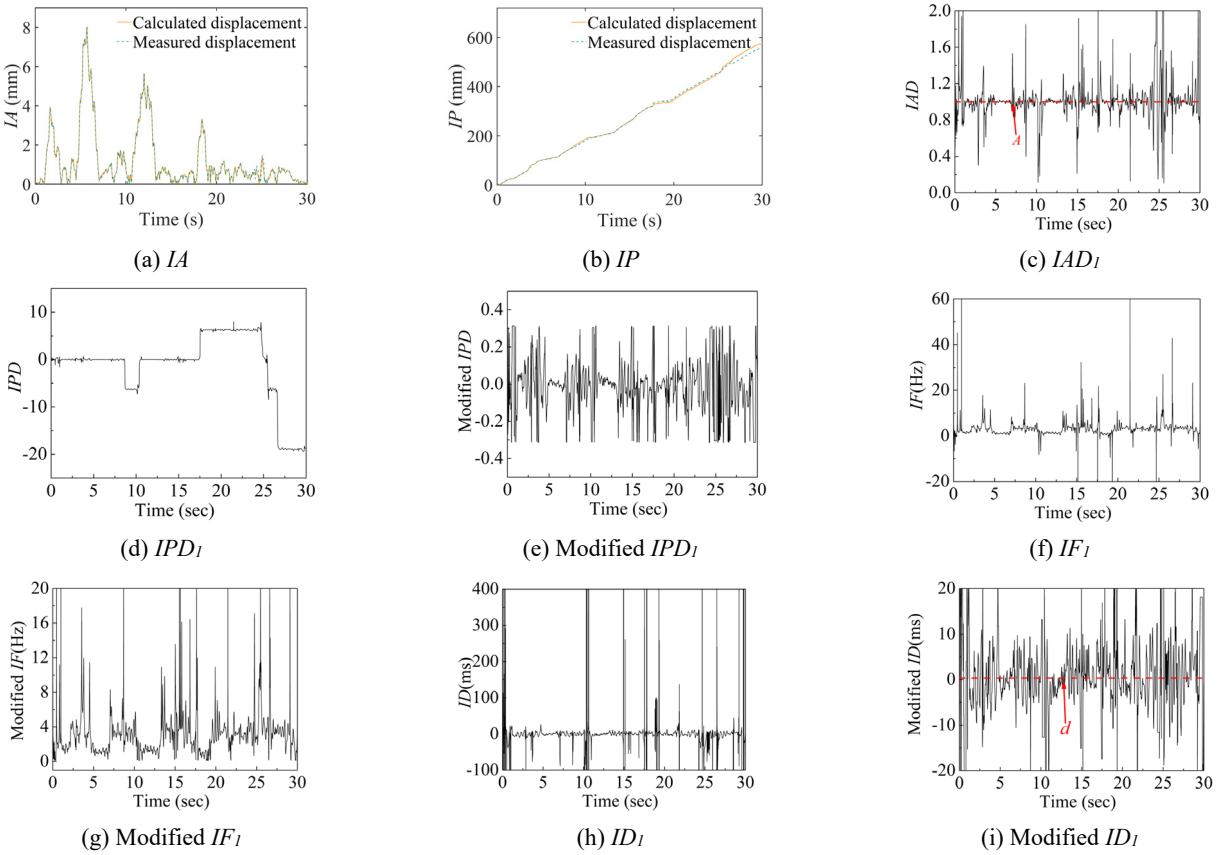

(a) IA (b) IP (c) IAD_1

(d) IPD_1 (e) Modified IPD_1 (f) IF_1

(g) Modified IF_1 (h) ID_1 (i) Modified ID_1

Fig. 13 ICPs obtained of IMF_1 using predefined displacement RTHS

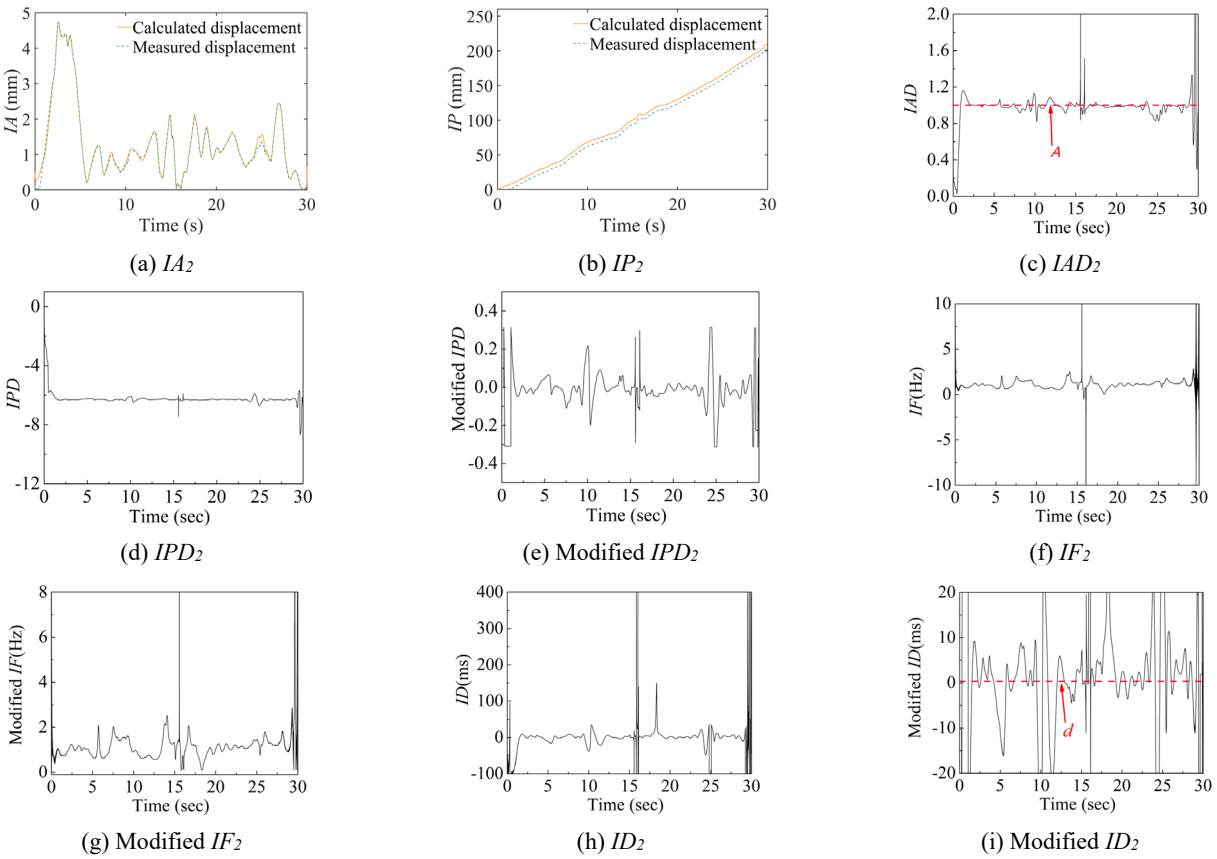

(a) IA_2 (b) IP_2 (c) IAD_2

(d) IPD_2 (e) Modified IPD_2 (f) IF_2

(g) Modified IF_2 (h) ID_2 (i) Modified ID_2

Fig. 14 ICPs obtained of IMF_2 using predefined displacement RTHS

red line A in Fig. 13(c). The IAD_1 reaches a maximum value of 10.4 at 24.66 s and a minimum value of 0.1 at 25.57 s, both occurring at points where IA_1 is extremely small. Excluding the initial moments of very small IA_1, most of the IAD_1 values cluster between 0.95 and 1.05, fluctuating around the FEI-calculated average amplitude A. Fig. 13(e) shows the computed IF_1 based on the IP_1 of the calculated displacement. The IF_1 values range from -106 Hz to 214 Hz, with the maximum value at 0.99 s and the minimum at 17.52 s. Fig. 13(f) shows the corrected IF_1, where negative frequencies have been removed. The R^{IF} is 97.34% (29902 points within range), indicating that 97.34% of IF_1 falls within this range. Fig. 13(g) shows the calculated ID_1, with values from -68 s to 14 s. The maximum and the minimum values occur at 0.11 s at 17.79 s, respectively, both corresponding to points with when very small IF_1. Fig. 13(h) shows the corrected ID_1, mostly fluctuating between -10 ms and 10 ms, with the average time delay d calculated by the FEI. This figure shows that the instantaneous time delay fluctuates around d, with an R^{ID} of 88.73% (27259 points within range).

IA_2 and IP_2 are shown in Figs. 14(a) and 14(b), where the clockwise amplitude corresponds to the maximum displacement over time. Figs. 14(c) and 14(d) show IAD_2 and IPD_2. According to the FEI analysis, the average amplitude for this simulation is 1.003, as indicated by the red line A in Fig. 14(c). The IAD_2 reaches a maximum of 47.12 at 29.62 s and a minimum of 0.03 at 0.46 s, both at moments of extremely small IA_2. Excluding the very small IA_2 at the beginning and end, most IAD_2 values fall between 0.95 and 1.05, fluctuating around the FEI- calculated average amplitude difference. Fig. 14(e) shows the computed IF_2 based on the IP_2 of the calculated displacement. The values of the IF_2 range from -20 Hz to 141 Hz, with the maximum value at 15.57 s and the minimum at 16.08 s. Fig. 14(f) shows the corrected IF_2, where negative frequencies are removed. The R^{IF} is 98.72% (30238 points in the range), indicating that 98.72% of the calculated IF_2 falls within this range. Fig. 14(g) shows the calculated ID_2, with values ranging from -24 s to 126 s. The maximum value occurs at 29.74 s and the minimum at 0.003 s, corresponding to moments when IF_2 is very small. Fig. 14(h) shows the corrected ID_2, excluding the beginning and end, mostly fluctuating between -10 ms and 10 ms. This figure also represents the average time delay d calculated by the FEI, showing that the instantaneous time delay fluctuates around d, with an R^{ID} of 92.15% (28,310 points within range).

Fig. 15(a) illustrates the displacement time histories of IMF_1 and IMF_2. As shown in Fig. 15(b), the IFs of IMF_1 and IMF_2 exhibit clear differences, with the frequency obtained from IMF_1 being slightly higher. This aligns with the fact that EMD decomposes a signal into different frequency components. The ICPs also vary across different frequency responses. As illustrated in Figs. 13(c) and 14(c), the IADs exhibit greater oscillations at higher frequencies,

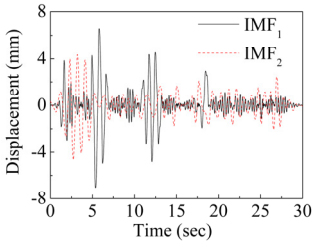

(a) Time history of displacement of each IMF

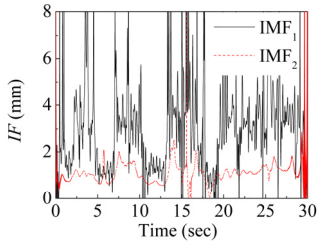

(b) *IF* of each IMF

Fig. 15 Time history and *IF* with different IMFs

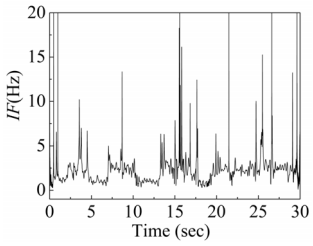

(a) *IF*

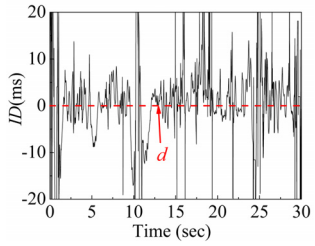

(b) *ID*

Fig. 16 ICPs using predefined displacement RTHS

Table 1 Comparison of effective R^{IF} of the two methods

	Traditional method	The new method based on EMD			Performance improvement
		IMF_1	IMF_2	The weighted results	
R^{IF}	92.95%	97.34%	98.72%	99.97%	7.02%

while they are more stable at lower frequencies. Similarly, as shown in Figs. 13(i) and 14(i), the ID follows the same pattern. An actuator's dynamic characteristics are frequency-dependent. Although these characteristics contribute to the same instantaneous time lag in the time domain, their behavior varies across different frequencies. As a time-frequency integration method, EMD allows us to extract not only the overall instantaneous time lag but also the instantaneous amplitude error and time lag at specific frequencies. Moreover, when the structure enters a nonlinear state, its frequency changes. Traditional methods can only capture the overall coupling of instantaneous control parameters across frequencies. In contrast, this method distinguishes ICPs at different frequencies, providing additional information for nonlinear compensation. This enables a more refined, segmental compensation approach.

Figs. 16(a) and 16(b) present the final weighted calculation of IF and ID. During the weighting calculation, if one of the IMFs is over the limit, its weight will be set to 0 and the other IMF will be set to 1. If both IMFs are over the limit, the result of the previous calculation will be used instead. With this benchmark, the IF or ID is considered unreliable only if both IMFs are over the limit. Finally, the R^{IF} is 99.97% and the R^{ID} is 96.45%.

In a predefined test with WFEI compensation, R^{IF} without EMD is 92.95%, R^{ID} is 92.9%. When applying EMD, IMF_1 calculates the R^{IF} of 97.34% and the R^{ID} of 88.73%, and IMF_2 calculates the R^{IF} of 98.72% and the R^{ID} of 92.15%. The weighted results showed the R^{IF} of 99.97%, a 7.02% improvement over no EMD, and the R^{ID} of 96.45%, a 3.55% improvement over no EMD. The refinement of effective parameters enables a more precise and detailed local evaluation in real-time hybrid simulation, leading to increasingly accurate insights into actuator tracking. This, in turn, offers valuable guidance for improving control strategies in real-time hybrid simulation. This indicates that EMD is beneficial.

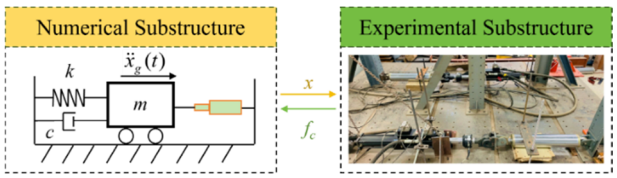

Fig. 17 Experimental substructure for RTHS

5. Experimental Verification through RTHS

5.1 Experimental setup and traditional ICP results for RTHS

The experimental setup and compensation method utilized are identical to those employed in the predefined displacement test. For the RTHS, the Single Degree of Freedom (SDOF) structure incorporating the self-centering viscous damper (SC-VD) device is illustrated in Fig. 17, with its equation of motion expressed as follows

$$m \cdot \ddot{x}(t) + c \cdot \dot{x}(t) + k \cdot x(t) + f_m(t) = -m \cdot \ddot{x}_g(t) \quad (8)$$

where the numerical substructure is characterized by a mass m of 1 kg, a stiffness k of 39.4784 N/m, and a viscous damping coefficient c of 0.2513 N/(m/s). The ground motion acceleration $\ddot{x}_g(t)$ from the PEER MU2035 dataset has a peak ground acceleration (PGA) of 3400 mm/s². Additionally, f_m represents the restoring force of the experimental substructure, specifically the SC-VD device. For the real-time hybrid simulation (RTHS), the numerical substructure is modeled using FRAME 2D (Castaneda *et al.* 2015). The unconditionally stable explicit CR algorithm is employed to solve the discretized equation of motion presented in Eq. (4), with an integration time step of 1/1024.

The applicability of the traditional ICP was validated by testing the RTHS for single-degree-of-freedom structures equipped with self-centering viscous dampers (Xu *et al.* 2024). Fig. 18(a) illustrates the RTHS test, with a detailed view of the 8.5 to 9-second interval provided in Fig. 18(b). To reduce the impact of high-frequency noise on subsequent calculations, zero-phase filtering was applied. Fig. 18(c) shows the *xc*-*xm* curve, showing a 45-degree straight line, and it is clear that *xc* has no significant phase difference from *xm*.

Figs. 19(c) and 19(d) present *IAD* and *IPD* are shown in. The analysis using the FEI yields an average amplitude of 1.01 for this simulation, as shown by the red line *A* in Fig. 19(c). The *IAD* reaches a maximum value of 1.53 at 23,80 s and a minimum value of *IAD* 0.02 at 2.58 s, both occurring at points where *IA* is extremely small. Excluding the initial moments of very small *IA*, most of the *IAD* values cluster between 0.95 and 1.05, fluctuating around the FEI-calculated average amplitude *A* calculated by the FEI.

Fig. 19(e) shows the computed *IF* based on the *IP* of the calculated displacement. The *IF* values range from -20 Hz

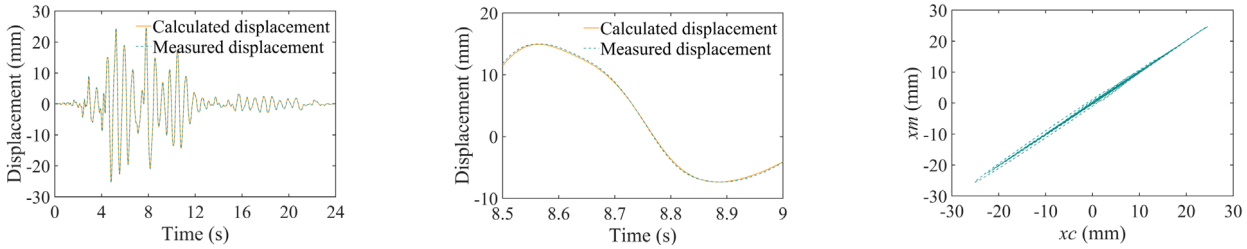

(a) Time history (b) Closed-up view of time history (c) *xc*-*xm* curve

Fig. 18 Time history of the original signal and the filtered post-signal

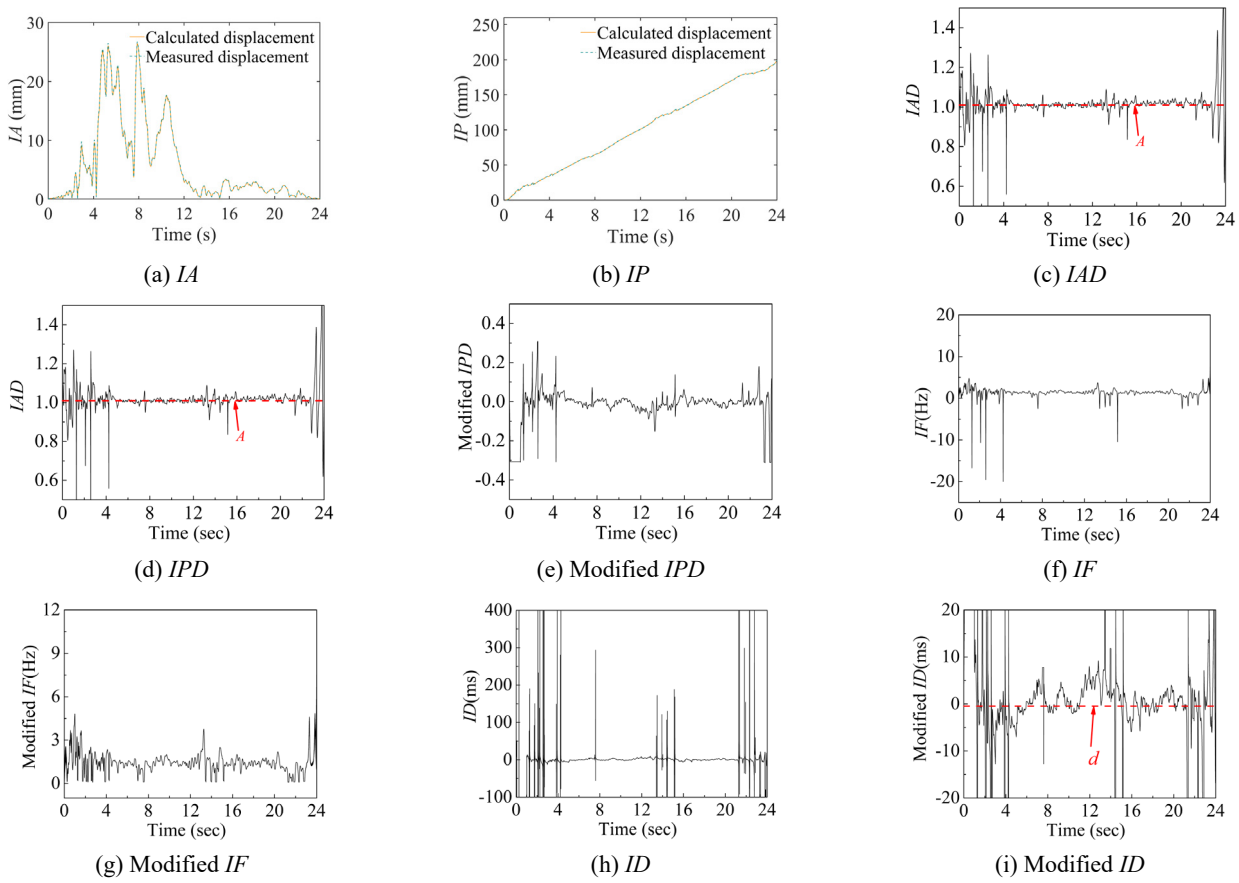

Fig. 19 Calculation using traditional ICP methods RTHS results

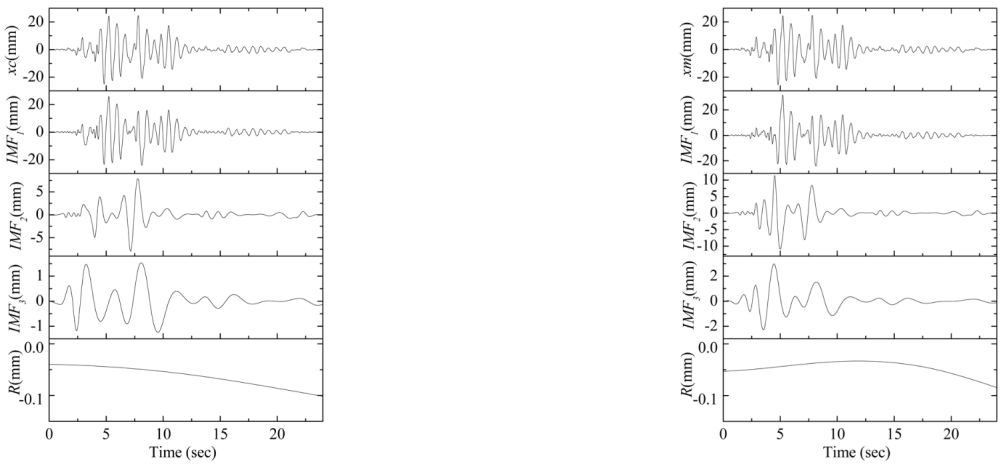

Fig. 20 IMFs obtained after EMD

to 35 Hz, with the maximum value at 24.00 s and the minimum at 4.25 s. Fig. 19(f) shows the corrected *IF*, where negative frequencies have been removed. The R^{IF} is 95.06% (23362 points within range), indicating that 95.06% of *IF* falls within this range. Fig. 19(g) shows the calculated *ID*, with values ranging from -99 s to 287 s. The maximum value occurs at 2.07 s and the minimum at 0.27 s, corresponding to moments when *IF* is very small. Fig. 19(h) shows the corrected *ID*, excluding the beginning and end, mostly fluctuating between -10 ms and 10 ms. This figure also represents the average time delay d calculated by the FEI, showing that the instantaneous time delay fluctuates around d, with an R^{ID} of 90.33% (22200 points within range).

5.2 RTHS with EMD

After EMD, *xc* produces 6 IMFs and *xm* produces 5 IMFs. Figs. 20(a) and 20(b) show 3 IMFs of the signals after EMD, and since the correlation coefficients of the

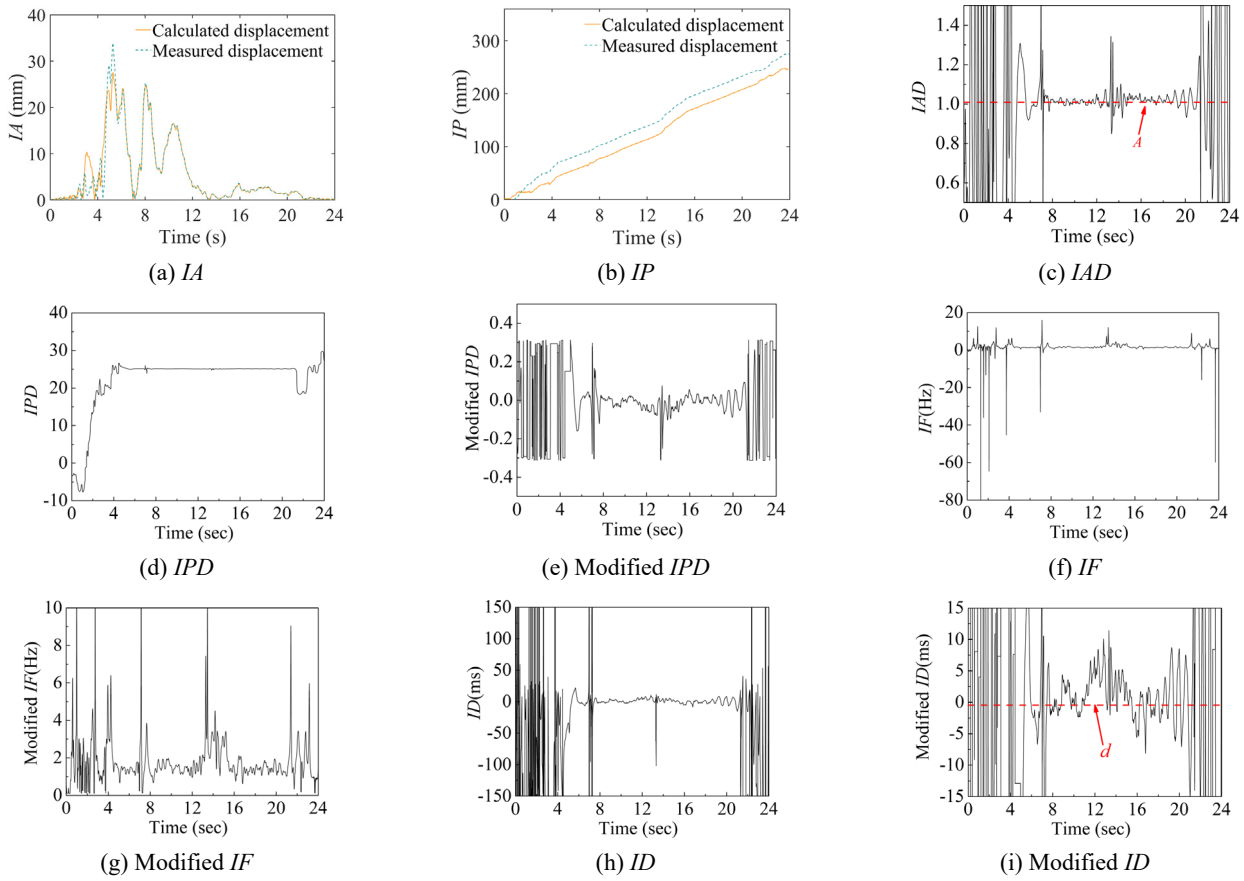

Fig. 21 ICPs obtained using RTHS test

Table 2 Comparison of effective R^{IF} of the two methods

	Traditional method	The new method based on EMD	Performance improvement
R^{IF}	95.06%	96.82%	1.76%

subsequent IMFs are too small, only 3 IMFs are shown, and the correlation coefficients of the three of these IMFs with the original signals are 0.955, 0.241, and 0.026, respectively. ultimately, only the first IMF is chosen for the perform the ICP calculation. The correlation coefficient between *xc* and *xm* is 0.999, the correlation coefficient between IMF_1 is 0.998, the correlation coefficient between IMF_2 is 0.956. This error is within the allowable range and EMD can be used.

Analysis using the FEI yielded an average amplitude difference and time delay of 1.01 and -0.47 ms, respectively. Figs. 21(a) and 21(b) present *IA* and *IP*. The *IP* shows significant asynchrony, which needs to be adjusted in subsequent calculations. The *IAD* and *IPD* are shown in Figs. 21(c) and 21(d). The FEI analysis yields an average amplitude of 1.01 in this simulation, as indicated by the red line *A* in Fig. 21(c). The *IAD* reaches a maximum value of 69.48 at 1.28 s and a minimum value 0.03 at 4.44 s. There is a clear error in the IAD calculation at both the beginning and end of the time period, stemming from the end- effects (Zare and Nouri 2023) of the EMD. The EMD process requires extreme points, which are determined through cubic spline interpolation. Without constraints at the endpoints, interpolation fails, leading to fictitious waves. As the IMF generation process operates in a continuous loop, the error becomes more pronounced with each iteration, increasing the wavelength of the erroneous signal. This results in a significant error due to the small signal displacement between the start and end time periods. Excluding the beginning and end of the time period, most *IAD* are concentrated between 0.95 and 1.05, fluctuating around the average amplitude difference *A* calculated by the FEI. The phase unfolding undergoes a significant asynchrony, which needs to be adjusted, and the range of the *IPD* is taken as [-π/10, π/10]. The modified *IPD* is shown in Fig. 21(e).

Fig. 21(f) shows the computed *IF* based on the *IP* of the calculated displacement. The *IF* values range from -160 Hz to 16 Hz, with the maximum value occurring at 7.13 s and the minimum value at 1.28 s. Fig. 21(g) shows the corrected *IF*, where the negative frequencies have been removed. The R^{IF} is 96.82% (23794 points within range), indicating that 96.82% of *IF* falls within range. Fig. 21(h) shows the calculated *ID*, with values from -2.36 s to 2.06 s. The maximum and the minimum values occurs at 3.77 s and 2.26 s, respectively, both corresponding to points with when

very small *IF*. Fig. 21(i) shows the corrected *ID*, excluding these periods of very small *IF*, mostly fluctuating from -5 ms to 10 ms, with the average time delay *d* calculated by FEI. This figure shows that the instantaneous time delay fluctuates around *d*, with an R^{ID} of 73.42% (18043 points within range).

The R^{IF} obtained without EMD was 95.06% and R^{ID} was 90.33%, after using EMD the R^{IF} increased to 96.82% and R^{ID} decreased to 73.42%. This suggests that EMD can improve the negative frequency problem to some extent, but some of the results after EMD may be counterproductive in cases where inheritance is not so good.

6. Conclusions

This study proposes a novel method based on EMD to enhance the calculation of ICPs. The effectiveness of the ICP methodology was validated through numerical simulations using a baseline model, and further verified through predefined displacement tests on a multi-degree-of-freedom structure with self-centering viscous dampers, as well as RTHS on a single-degree-of-freedom structure at the laboratory of Southeast University. Based on the analyses and discussions presented, the following conclusions can be drawn:

- **A calculation method based on EMD is employed to determine ICPs:** The traditional ICP calculation method is plagued by negative frequencies, and EMD can provide a certain degree of solution to this problem. The method of EMD is used to decompose the original signal into a series of IMFs, combine the matched IMFs to calculate the ICP, and weight them to get the result.
- **EMD-Based Calculation of ICPs:** This study employs an EMD-based method for determining ICPs. Traditional ICP calculation methods often generate negative frequencies, but EMD offers a partial solution to this issue. The approach involves decomposing the original signal into a set of IMFs, selecting the IMFs that best match the ICP, and applying weighted aggregation to obtain the final ICP result.
- **IMF Matching and Weighting Methodology:** A new approach for matching and weighting IMFs is proposed to handle multiple calculated and measured displacements following EMD. Directly using all IMFs in ICP calculations is infeasible due to signal complexity; thus, this method establishes a one-to-one correspondence between displacements and their associated IMFs using correlation coefficients. Additionally, a weighting scheme is introduced, adjusting each set of ICPs based on the correlation strength between the original signal and the corresponding IMF.
- **Recommendations for EMD Use:** The correlation coefficients between decomposed, matched IMFs and the original signal are evaluated. If the error exceeds 5%, the EMD method is not recommended, as large discrepancies indicate a poor inheritance of the original signal's characteristics in the decomposed IMFs.
- **Numerical Simulation and Experimental test Validations:** Numerical simulations validate the reliability of the ICP calculations. Experimental results indicate that for signals with multiple extreme points between zero-crossings, traditional calculation methods introduce numerous negative frequencies. The EMD approach, however, significantly mitigates this issue, yielding more accurate results.
- **Importance of the new method based on EMD:** Although the effective parameters of the ICP computed using the new method show only minor improvements, these refinements enable a more precise local evaluation and offer stronger support for adaptive compensation strategies. Additionally, as a time-frequency integration method, EMD allows for the extraction of not only the overall ICP but also the ICP at different frequencies. This offers valuable insights into the frequency-dependent dynamic characteristics of the actuator and presents the potential for segmental compensation as the structure transitions into a nonlinear state.
- **Challenges with IMF Accuracy and Instantaneous Frequency Calculation:** IMFs generated through EMD exhibit considerable errors at the signal boundaries due to end-effects. Furthermore, direct application of the Hilbert transform for instantaneous frequency calculations is restricted by the Bedrosian and Nuttall theorems, often causing notable discrepancies between computed and actual instantaneous frequencies. This limitation hinders precise time-frequency analysis of nonlinear and nonstationary signals, and future research will focus on addressing these challenges to enhance the robustness of the EMD-based ICP calculation approach.

Acknowledgments

The first author would like to acknowledge the support from National Science Foundation of China under Grant No. 52178114 and 51808111.

References

Castaneda, N., Gao, X. and Dyke, S.J. (2015), "Computational tool for real-time hybrid simulation of seismically excited steel frame structures", *J. Comput. Civil Eng.*, **29**(3), p. 04014049. https://doi.org/doi:10.1061/(ASCE)CP.1943-5487.0000341

Chang, S.-Y. (2002), "Explicit pseudodynamic algorithm with unconditional stability", *J. Eng. Mech.*, **128**(9), 935-947. https://doi.org/doi:10.1061/(ASCE)0733-9399(2002)128:9(935)

Chen, C. and Ricles, J.M. (2008), "Development of direct integration algorithms for structural dynamics using discrete control theory", *J. Eng. Mech.*, **134**(8), 676-683. https://doi.org/doi:10.1061/(ASCE)0733-9399(2008)134:8(676)

Condori Uribe, J.W., Salmeron, M., Patino, E., Montoya, H., Dyke, S.J., Silva, C.E., Maghareh, A., Najarian, M. and Montoya, A. (2023), "Experimental benchmark control problem for multi-axial real-time hybrid simulation", *Front. Built*

Environ., **9**, p. 2070996. https://doi.org/10.3389/fbuil.2023.1270996

Gabor, D. (1947), "Theory of communication", *J. Institut. Electr. Engr. - Part I*: *General*, **94**(73), 58-58. https://doi.org/10.1049/ji-1.1947.0015

Gao, Q., Duan, C., Fan, H. and Meng, Q. (2008), "Rotating machine fault diagnosis using empirical mode decomposition", *Mech. Syst. Signal Process*., **22**(5), 1072-1081. https://doi.org/10.1016/j.ymssp.2007.10.003

Guo, T., Chen, C., Xu, W. and Sanchez, F. (2014), "A frequency response analysis approach for quantitative assessment of actuator tracking for real-time hybrid simulation", *Smart Mater. Struct*., **23**(4), p. 045042. https://doi.org/10.1088/0964-1726/23/4/045042

Guo, Y., Bao, Y., Li, H. and Zhang, Y. (2023), "Deep learning-based adaptive mode decomposition and instantaneous frequency estimation for vibration signal", *Mech. Syst. Signal Process*., **199**, p. 110463. https://doi.org/10.1016/j.ymssp.2023.110463

Hayati, S. and Song, W. (2017), "An optimal discrete-time feedforward compensator for real-time hybrid simulation", *Smart Struct. Syst*., *Int. J*., **20**(4), 483-498. https://doi.org/10.12989/sss.2017.20.4.483

Horiuchi, T., Inoue, M., Konno, T. and Namita, Y. (1999), "Real-time hybrid experimental system with actuator delay compensation and its application to a piping system with energy absorber", *Earthq. Eng. Struct. Dyn*., **28**(10), 1121-1141. https://doi.org/10.1002/(SICI)1096-9845(199910)28:10

Huang, N.E., Shen, Z., Long, S.R., Wu, M.C., Shih, H.H., Zheng, Q., Yen, N.C., Tung, C.C. and Liu, H.H. (1998), "The empirical mode decomposition and the Hilbert spectrum for nonlinear and non-stationary time series analysis", *Proceedings of the Royal Society of London. Series A*: *Mathematical*, *Physical and Engineering Sciences*, **454**(1971), 903-995. https://doi.org/doi:10.1098/rspa.1998.0193

Huang, N.E., Wu, Z., Long, S.R., Arnold, K.C., Chen, X. and Blank, K. (2009), "On instantaneous frequency", *Adv. Adapt. Data Anal*., **01**(02), 177-229. https://doi.org/10.1142/s1793536909000096

Huang, L., Chen, C., Huang, S. and Wang, J. (2022), "Stability of real-time hybrid simulation involving time-varying delay and direct integration algorithms", *J. Vib. Control*, **28**(13-14), 1818-1834. https://doi.org/10.1177/10775463211001618

Li, N., Teng, X. and Zhou, Z. (2024), "Quantitative analysis of time-varying delay for real-time hybrid simulation", *J. Vib. Control*, **30**(3-4), 673-684. https://doi.org/10.1177/10775463221149766

López, C. and Moore, K.J. (2024), "Enhanced adaptive linear chirplet transform for crossing frequency trajectories", *J. Sound Vib*., **578**, p. 118358. https://doi.org/https://doi.org/10.1016/j.jsv.2024.118358

Maiti, R., Menon, B.G. and Abraham, A. (2024), "Ensemble empirical mode decomposition based deep learning models for forecasting river flow time series", *Expert Syst. Applicat*., **255**, p. 124550. https://doi.org/https://doi.org/10.1016/j.eswa.2024.124550

Mosqueda, G., Stojadinovic, B. and Mahin, S.A. (2007), "Real-time error monitoring for hybrid simulation. Part I: methodology and experimental verification", *J. Struct. Eng*., **133**(8), 1100-1108. https://doi.org/doi:10.1061/(ASCE)0733-9445(2007)133:8(1100)

Nakashima, M., Kato, H. and Takaoka, E. (1992), "Development of real-time pseudo dynamic testing", *Earthq. Eng. Struct. Dyn*., **21**(1), 79-92. https://doi.org/10.1002/eqe.4290210106

Nakata, N. and Stehman, M. (2014), "Compensation techniques for experimental errors in real-time hybrid simulation using shake tables*Syst*., *Int. J*., **14**(6), 1055-1079. https://doi.org/10.12989/sss", *Smart Struct*..2014.14.6.1055

Park, J., Pao, G.M., Sugihara, G., Stabenau, E. and Lorimer, T. (2022), "Empirical Mode Modeling: A data-driven approach to recover and forecast nonlinear dynamics from noisy data", *Nonlinear Dyn*., **108**(3), 2147-2160. https://doi.org/10.1007/s11071-022-07311-y

Phillips, B.M., Takada, S., Spencer Jr, B.F. and Fujino, Y. (2014), "Feedforward actuator controller development using the backward-difference method for real-time hybrid simulation", *Smart Struct. Syst*., *Int. J*., **14**(6), 1081-1103. https://doi.org/10.12989/sss.2014.14.6.1081

Shirdade, N., Kolliyil, J.J., El-Khader, B.A.D.T. and Brindise, M.C. (2024), "Characterizing the onset of transitional and turbulent flow regimes in pipe flows using instantaneous time-frequency-based analysis", *Phys. Fluids*, **36**(10). https://doi.org/10.1063/5.0226070

Stavridis, A. and Shing, P.B. (2010), "Hybrid testing and modeling of a suspended zipper steel frame", *Earthq. Eng. Struct. Dyn*., **39**(2), 187-209. https://doi.org/10.1002/eqe.940

Van der Pol, B. (1946), "The fundamental principles of frequency modulation", *J. Inst. Electr. Engr. - Part III*: *Radio Commun. Eng*., **93**(23), 153-158. https://doi.org/10.1049/ji-3-2.1946.0024

Van Jaarsveldt, C., Peters, G.W., Ames, M. and Chantler, M. (2023), "Tutorial on empirical mode decomposition: Basis decomposition and frequency adaptive graduation in non-stationary time series", *IEEE Access*, **11**, 94442-94478. https://doi.org/10.1109/ACCESS.2023.3307628

Wang, Y., Guo, W., Liang, X., Huang, R., He, X. and Rao, Z. (2024), "Boundary coordination algorithm for real-time hybrid test of high-speed maglev train-guideway coupling vibration", *Eng. Struct*., **314**, p. 118355. https://doi.org/10.1016/j.engstruct.2024.118355

Xu, G., Ning, X., Huang, W., Wang, Z. and Zheng, L. (2023), "Validation of model-based adaptive control method for real-time hybrid simulation", *Smart Struct. Syst*., *Int. J*., **31**(3), 259-273. https://doi.org/10.12989/sss.2023.31.3.259

Xu, W., Peng, C., Guo, T. and Chen, C. (2024), "Exploration of instantaneous frequency for local control assessment in real-time hybrid simulation", *Earthq. Eng. Eng. Vib*., **23**, 1-14. https://doi.org/10.1007/s11803-024-2284-2

Zare, M. and Nouri, N.M. (2023), "End-effects mitigation in empirical mode decomposition using a new correlation-based expansion model", *Mech. Syst. Signal Process*., **194**, p. 110205. https://doi.org/10.1016/j.ymssp.2023.110205